Journal of
Synchrotron
Radiation

ISSN 1600-5775

Received 29 August 2014
Accepted 24 November 2014

Noncrystalline structure of Ni–P nanoparticles prepared by liquid pulse discharge

Yuanyuan Tan,[a] Hongying Yu,[b] Zhonghua Wu,[c]* Bin Yang,[a] Yu Gong,[c] Shi Yan,[a,c] Rong Du,[c] Zhongjun Chen[c] and Dongbai Sun[a]*

[a]National Center for Materials Service Safety, University of Science and Technology Beijing, Beijing 100083, People's Republic of China, [b]Corrosion and Protection Center, Laboratory for Corrosion-Erosion and Surface Technology, University of Science and Technology Beijing, Beijing 100083, People's Republic of China, and [c]Institute of High Energy Physics, Chinese Academy of Sciences and Graduate University of Chinese Academy of Sciences, Beijing 100049, People's Republic of China. *E-mail: wuzh@ihep.ac.cn, dbsun@mater.ustb.edu.cn

Noncrystalline nickel phosphide (Ni–P) nanoparticles have drawn great attention due to their high potential as catalysts. However, the structure of noncrystalline Ni–P nanoparticles is still unknown, which may shed light on explaining the catalysis mechanism of the Ni–P nanoparticles. In this paper, noncrystalline Ni–P nanoparticles were synthesized. Their morphology, particle size, element contents, local atomic structures, as well as the catalysis in the thermal decomposition of ammonium perchlorate were studied. The results demonstrate that the as-prepared Ni–P nanoparticles are spherical with an average diameter of about 13.5 nm. The Ni and P contents are, respectively, 78.15% and 21.85%. The noncrystalline nature of the as-prepared Ni–P nanoparticles can be attributed to cross-linkage between P-doping f.c.c.-like Ni centers and Ni_3P-like P centers. The locally ordered Ni centers and P centers are the nuclei sites, which can explain well the origin of initial nuclei to form the crystalline phases after high-temperature annealing. The starting temperature of high-temperature decomposition of ammonium perchlorate was found having a significant decrease in the presence of the noncrystalline Ni–P nanoparticles. Therefore, the as-prepared noncrystalline Ni–P nanoparticles can be used as a potential catalyst in the thermal decomposition of ammonium perchlorate.

Keywords: noncrystalline structure; Ni–P nanoparticles; pulse discharge; local structure model.

© 2015 International Union of Crystallography

1. Introduction

Transition metal phosphides have attracted wide interest due to their excellent properties including catalytic activity (Oyama *et al.*, 2009), magneto-caloric effect (Tegus *et al.*, 2002), magneto-resistance (Jiang & Kauzlarich, 2006) and Li intercalation behavior (Souza *et al.*, 2002; Mauvernay *et al.*, 2006). In particular, transition metal phosphides could be used as a catalyst in the thermal decomposition of ammonium perchlorate (AP). It is well known that AP is a key energetic material for rocket technologies (Vyazovkin & Wight, 1999; Boldyrev, 2006). As a main oxidizing agent, AP has been widely used in various propellants. The combustion behavior of propellants is highly relevant to the thermal decomposition process of AP. The ballistics of a composite propellant can be improved by addition of a catalyst, such as metal oxides (Li *et al.*, 2008; Wang *et al.*, 2005) and metal nanoparticles (Wang *et al.*, 2013). A previous study (Liu *et al.*, 2004) reported that nanoscale metals (for instance Ni, Cu, Al and NiCu powders) improved significantly the AP decomposition efficiency, and these nanoscale metals were oxidized into the corresponding metal oxides by the oxidizing gases O_2, NO and N_2O released during AP decomposition. It was also expected that Ni–P alloy nanoparticles, as a potential catalyst (Zhao *et al.*, 2010), can speed the decomposition course or change the decomposition temperature of AP. In particular, it was claimed that the amorphous nature (Burchardt *et al.*, 2001) of Ni–P nanoparticles enhanced their catalytic activity in a hydrogen evolution reaction. Therefore, noncrystalline Ni–P nanoparticles are expected to have better catalytic activity toward AP decomposition.

It is well known that the catalytic performance is strongly dependent on the size, morphology and microstructure of catalyst particles. On the one hand, the decrease of particle size (Kang *et al.*, 2014) can increase sharply the catalytic efficiency. On the other hand, the high-order planes (Tian *et al.*, 2007) presented on the particle surface can also extremely improve the catalytic activity. Therefore, controlling the size

and morphology of catalyst particles is one of the main research interests for catalyst study. For this purpose, multiple synthesizing routes of Ni–P nanoparticles with various shapes (solid particles, core-shell particles, rods and wires) have been reported in recent years; for example, the solid phase reaction (Shi & Shen, 2009), the solution phase reaction (Elayaraja *et al.*, 2011; Zheng *et al.*, 2009*a*,*b*; Chen *et al.*, 2009), the decomposition of single source precursors (Maneeprakorn *et al.*, 2009), the thermolysis of nickel compounds (Wang *et al.*, 2009) and so on. A relatively inexpensive synthesis method (Mandel *et al.*, 2011) was also developed. However, the modulation for the microstructure of catalyst particles is also an important route to improve their catalytic performance. Although it is not easy to change optionally the crystalline structures of catalyst particles, it is still a possible route to improve the catalytic performance by controlling the noncrystalline nature of catalyst particles.

Undoubtedly, microstructural study on noncrystalline Ni–P nanoparticles is helpful to understand better their performance and the catalytic mechanism. Extended X-ray absorption fine-structure (EXAFS) spectroscopy is a powerful technique to probe the local atomic structure. In particular, the EXAFS technique is suitable for the structure study of noncrystalline nanoparticles with only short-range-ordered structure. There have been some EXAFS investigations for Ni_2P catalyst prepared under different conditions (Oyama, 2002; Kawai *et al.*, 2005, 2006). The active site (Oyama *et al.*, 2009; Oyama & Lee, 2008) of nickel phosphide catalysts for hydrodesulfurization was characterized by the EXAFS technique. An unintended phosphorus doping (Moreau *et al.*, 2012) in the nickel nanoparticles was reported from the EXAFS analysis. However, the structural description of noncrystalline nickel phosphide nanoparticles is still scarce because of the complexity of noncrystalline structures and the shortage of long-range-ordered structures.

In this paper, the local atomic structures of noncrystalline Ni–P nanoparticles will be probed from both Ni *K*-edge and P *K*-edge EXAFS spectra. The catalytic activity of the as-prepared Ni–P nanoparticles will be measured. Based on the experimental results, a structural model of the noncrystalline Ni–P nanoparticles will be proposed, which is expected to be helpful in the exploitation of more effective and cheaper Ni–P catalysts.

2. Experiments

2.1. Synthesis of noncrystalline Ni–P nanoparticles

Nickel phosphide nanoparticles were prepared by using a liquid-phase pulse-discharge method. Nickel sulfate with six structural waters ($NiSO_4{\cdot}6H_2O$) and sodium hypophosphite with one structural water ($NaH_2PO_2{\cdot}H_2O$) were used as reactants, which were dissolved in distilled water to form the reaction solution with $NiSO_4{\cdot}6H_2O$ molar concentration of 2 *M* and $NaH_2PO_2{\cdot}H_2O$ molar concentration of 1 *M*. After the reaction solution was heated to 85°C, 60 pulse-discharges were released into the solution to trigger the chemical reaction. At almost the same time, the reaction solution gradually turned black. After cooling down, the black solution was collected into centrifuge tubes for centrifugal separation. Then, black nickel phosphide nanoparticles were obtained by drying the deposit at 45°C for 4 h. A more detailed synthesis process has been described elsewhere (Tan *et al.*, 2014*a*).

2.2. Structural characterizations

2.2.1. TEM observations. The as-prepared Ni–P nanoparticles were re-dispersed into ethanol to form a suspension. One drop of this suspension was dropped on a carbon-coated copper grid. After evaporation of the solvent, a TECNAI F-30 transmission electron microscope (TEM) was used to observe the morphology of the as-prepared Ni–P nanoparticles. In addition, energy-dispersive X-ray spectroscopy (EDS) was also collected for the composition analysis of the nanoparticles. In order to observe further details of the particles, a high-resolution TEM image was also collected using a Jeol-2010 microscope.

2.2.2. XRD patterns. Powder X-ray diffraction (XRD) data of the as-prepared Ni–P nanoparticles were collected at the XRD station of beamline 4B9A at the Beijing Synchrotron Radiation Facility (BSRF) under ambient conditions (25°C). The incident X-ray wavelength was chosen as 1.54 Å. The data collection time of each XRD pattern (sample with and without annealing) was about 2 h.

2.2.3. XAFS spectra. XAFS spectra of the Ni–P nanoparticles were collected at BSRF. The storage ring was run at 2.5 GeV with an electron current of about 100 mA. Ni *K*-edge XAFS measurements were carried out at beamline 4B9A. A double-crystal Si(111) monochromator was used to choose the incident X-ray energy with an energy resolution ($\Delta E/E$) of about 2×10^{-4}. The Ni *K*-edge XAFS spectra were collected in transmission mode with a scanning energy range from 8133 to 9133 eV. The incident and transmission X-ray intensities were collected with ion chambers. The P *K*-edge XAFS data were collected at beamline 4B7A. The incident X-ray energy was also chosen using a double-crystal Si(111) monochromator. The Ni–P powder samples were smeared onto carbon adhesive tape, which was mounted in a vacuum chamber for XAFS measurements. The P *K*-edge XAFS spectra were collected in fluorescence mode with a scanning energy range from 2100 to 2754 eV. The fluorescence signal was collected with a Si(Li) detector. These XAFS data of the Ni and P *K*-edges were analyzed by using the software *IFEFFIT*-1.2.11 (University of Chicago, USA). The reference spectra of the Ni and P *K*-edges were calculated by using the *FEFF8* code (University of Washington, USA).

2.3. Catalytic performance

In order to characterize the catalytic performance of the as-prepared Ni–P nanoparticles, two samples (pure AP and AP with Ni–P nanoparticles) were prepared. The content of the Ni–P nanoparticles was 8.5 wt% in the AP sample with Ni–P nanoparticles. The thermal decomposition processes of AP with and without Ni–P nanoparticles were studied by using

differential scanning calorimetry (DSC). DSC measurements were performed over a temperature range of 50–600°C by using DTA404PC. The heating rate was 10°C min^{-1}. The samples were sealed in a closed pan, and the pan was swept by an Ar-flow at a rate of 150 ml min^{-1}. The total masses were 6.8 mg for both samples with and without Ni–P nanoparticles in the DSC measurements.

3. Results and discussion

A TEM micrograph of the as-prepared Ni–P nanoparticles is shown in Fig. 1(*a*). It can be seen that the particle shape is approximately spherical with an average particle size of about 13.5 nm. The EDS spectrum of the as-prepared Ni–P nanoparticles is shown in Fig. 1(*b*). Four elements, P, Ni, C and Cu, are revealed by the EDS spectrum. C and Cu elements can be excluded from the source materials and the synthesis process. Obviously, both C and Cu can be attributed to the TEM sample holder of carbon-coated copper grids. After excluding the contribution of C and Cu, it can be concluded that the as-prepared nanoparticles are composed only of Ni and P elements. The atomic percentages of Ni and P are calculated to be 72.2 at% and 27.8 at%, respectively. More accurate composition analysis was also performed using inductively coupled plasma-mass spectroscopy (ICP-MS). The result shows that the as-prepared Ni–P nanoparticles contain 78.1 (±0.3) at% Ni and 21.9 (±0.2) at% P. The chemical compositions obtained from ICP-MS and EDS are apparently a little different. Owing to the higher statistics of ICP-MS compared with EDS, the results obtained from ICP-MS are more reliable.

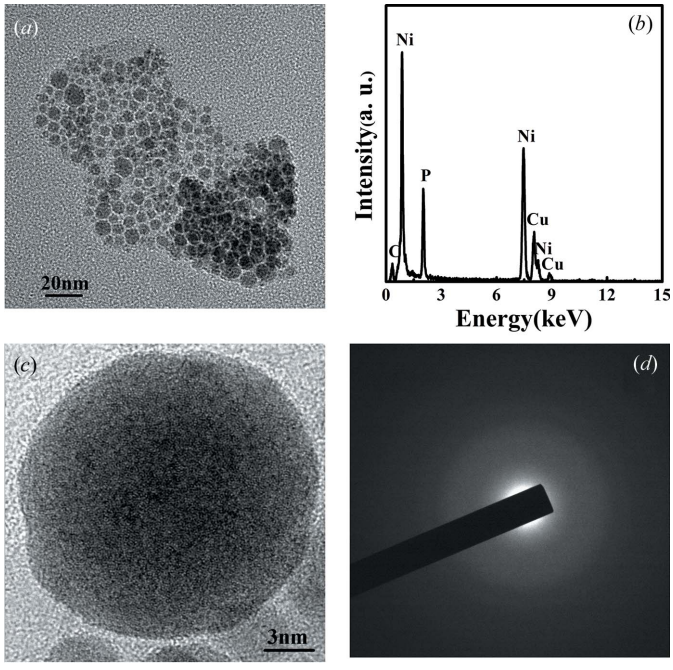

Figure 1
TEM micrograph (*a*), EDS spectrum (*b*), high-resolution TEM image (*c*), and electron diffraction pattern (*d*) of the as-prepared Ni–P nanoparticles synthesized by the liquid-phase pulsed-discharge method.

A high-resolution TEM (HRTEM) image of an as-prepared Ni–P nanoparticle is shown in Fig. 1(*c*). It can be seen that there is no obvious long-range-ordered structure except the specious contrast difference at some local sites of the HRTEM image. The HRTEM image indicates that the as-prepared Ni–P nanoparticles are in a noncrystalline state. In order to validate the noncrystalline structure of the as-prepared Ni–P nanoparticles, their electronic diffraction pattern was also collected as shown in Fig. 1(*d*). Evidently, there are no obvious diffraction rings or diffraction spots appearing on the pattern, verifying further the noncrystalline nature of the as-prepared Ni–P nanoparticles.

A room-temperature XRD pattern of the as-prepared Ni–P nanoparticles was also collected, as shown in Fig. 2. Different from the TEM diffraction pattern, two diffuse and weak diffraction peaks can be distinguished from the XRD pattern. For a homogeneous amorphous system, its XRD pattern presents commonly a wide diffuse peak. However, an additional high-order diffraction peak is also appearing in the XRD pattern of the Ni–P nanoparticles, although its diffraction intensity is quite weak. The appearance of the second diffraction peak implies that some imperfect short-range- or intermediate-range-ordered structures actually exist in some local sites of the nanoparticles. It is due to the higher statistical counts in the XRD pattern than in the TEM diffraction pattern and the contrast difference between both techniques; the second diffuse peak was observed by XRD. Unfortunately, this XRD pattern cannot be used to refine the imperfect short-range- or intermediate-range-ordered structures in the as-prepared Ni–P nanoparticles. It is well known that the possible crystalline phases consisting of Ni and P include Ni_3P, Ni_2P, $Ni_{12}P_5$, pure Ni and so on. By comparison, the XRD pattern of pure Ni (JCPDS65-2865) is most similar to the room-temperature XRD pattern of the nanoparticles as shown in Fig. 2. Roughly, the first diffuse peak around 45° in Fig. 2 can be partially attributed to the co-contribution of (111) and

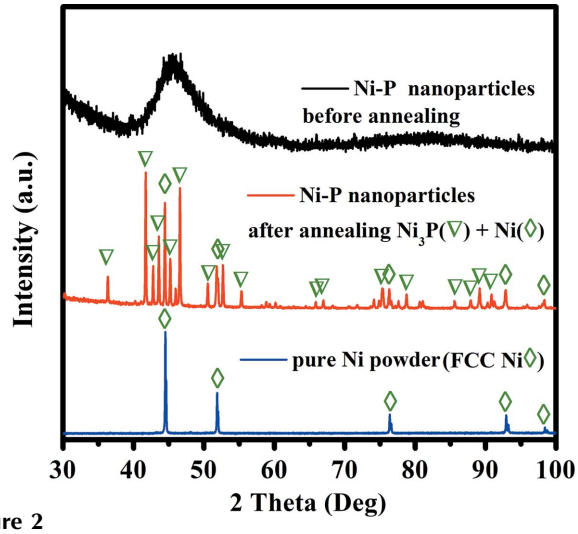

Figure 2
X-ray diffraction patterns before and after the as-prepared Ni–P nanoparticles were annealed at high temperature. The final crystalline phases were Ni_3P (JCPDS 34-501) and Ni (JCPDS 65-2865).

(200) reflections in a face-centered-cubic (f.c.c.)-like structure; the second diffuse peak around 82°can be attributed to the co-contribution of (220) and (311) reflections in the same f.c.c.-like structure. Although these Ni–P nanoparticles cannot be classified in the crystalline phase, they can be still considered to have distorted and f.c.c.-like short-range- or intermediate-range-ordered structures. Some tiny Ni–P clusters with Ni_3P-like (JCPDS 34-0501) distorted local structure could also make a contribution to the diffuse peaks. Evidently, a diffuse peak in the amorphous phase corresponds to the contribution of coherent scattering, while the coherent scattering of an amorphous sample comes merely from the locally ordered regions. In principle, the average size of the locally ordered regions can be evaluated from the width of the diffuse peak by using the Debye–Scherrer formula. For the amorphous Ni–P nanoparticles, the average size of the locally ordered regions was evaluated to be about 1.8 nm from the first diffuse peak. This evaluated size (∼1.8 nm) represents only a spatial dimension to maintain the coherent scattering in the amorphous network of the as-prepared Ni–P nanoparticles. Obviously, the dimension evaluated from the XRD pattern is much smaller than the Ni–P particle size as observed by TEM (13.5 nm). On average, each Ni–P nanoparticle consists of about 400 locally ordered regions. In fact, these locally ordered regions cannot be considered as a simple stacking of isolated clusters in a particle. In other words, the Ni atoms tend to form a f.c.c.-like ordered structure, but the entrance of P atoms causes serious structural distortion. Therefore, the locally ordered regions can only be maintained in the local environment. In these locally ordered regions, the coordination environment around Ni atoms forms P-doped f.c.c.-like Ni centers and the coordination environment around P atoms forms Ni_xP-like P centers. These Ni centers and P centers are randomly linked together through bondings. It is the cross-linkage of tiny Ni centers and P centers that form a noncrystalline network in the Ni–P nanoparticles. Based on this hypothesis of noncrystalline Ni–P nanoparticles, both the P-doped f.c.c.-like Ni centers and the Ni_xP-like P centers can be considered as the initial nucleation sites in the noncrystalline nanoparticles. When these noncrystalline Ni–P nanoparticles are heated to high temperature, some new phases (crystal nuclei) of P-doped f.c.c.-like Ni and Ni_xP compounds will form and grow. In order to validate this local structure hypothesis for the as-prepared Ni–P nanoparticles, the as-prepared Ni–P nanoparticles were annealed at 700°C for 2 h. Their XRD pattern was also collected at beamline 4B9A at the BSRF as shown in Fig. 2. It can be seen that these Ni–P nanoparticles were completely crystallized into P-doped f.c.c.-Ni and Ni_3P phases after annealing. A crystallization process study (Tan *et al.*, 2014*b*) for the noncrystalline Ni–P nanoparticles had been performed at a number of intermediate temperatures. The results demonstrated that the P-doped f.c.c.-Ni and Ni_3P phases as well as a metastable phase were simultaneously observed when the annealing temperature was raised to 300°C, but the content of the metastable phase was only about 2% and was almost unchangeable until it disappeared at 700°C. However, the Ni_3P phases were first grown to saturation content (∼55%) with the annealing temperature increasing to 350°C; the P-doped f.c.c.-Ni phase increased gradually and the amorphous matrix decreased gradually with the increase of the annealing temperature. During the formation process of both Ni_3P and P-doped f.c.c.-Ni phases, the locally ordered P centers were transformed faster to stoichiometric Ni_3P crystal nuclei by moving out excessive Ni atoms from the P centers. The locally ordered Ni centers were gradually transformed to P-doped f.c.c.-Ni crystal nuclei by moving out the excessive P atoms from the Ni centers. Simultaneously, the excessive Ni and P atoms excluded from the Ni_3P and the P-doped f.c.c.-Ni crystal nuclei were temporarily transformed to the metastable phase. These results illustrate that the initial nucleation sites in the noncrystalline Ni–P nanoparticles are indeed the locally ordered P-doped f.c.c.-like Ni centers and the locally ordered Ni_3P-like P centers. Therefore, the noncrystalline Ni–P nanoparticle can be described as a 'complex' of P-doped f.c.c.-like Ni centers and Ni_3P-like P centers. Namely, the noncrystalline Ni–P nanoparticle includes random-stacking P-doped Ni and Ni_3P crystal nuclei. These tiny nuclei are cross-linked together to form the noncrystalline Ni–P network.

To validate further the structural hypothesis about the as-prepared noncrystalline Ni–P nanoparticles, the XAFS technique was used to detect the local atomic structure. Ni *K*-edge XAFS spectra of the as-prepared Ni–P nanoparticles and the pure Ni foil were collected. For comparison, the Ni *K*-edge XAFS spectrum of Ni_3P was also calculated based on its crystal structure (Watanabe *et al.*, 2001). All three Ni *K*-edge XAFS spectra are compared in Fig. 3(*a*), and an enlarged image near the absorption edge of the three spectra is displayed in Fig. 3(*b*). Roughly, the XAFS spectrum of the as-prepared Ni–P nanoparticles has much larger disorder and less oscillation details. To a certain extent, its XAFS spectrum has similar spectral features as the Ni foil, but it is only similar and not the same as that of Ni foil due to the P-atom entrance into the f.c.c.-like lattice. In the same way, the XAFS spectrum of the as-prepared Ni–P nanoparticles also displays some comparability with the calculated XAFS spectrum of the Ni_3P crystal. However, it can be found that the as-prepared Ni–P nanoparticles and the Ni foil have only one nearest-neighbor coordination peak, but the nearest-neighbor coordination peak around Ni centers is completely split into two sub-peaks for the crystalline Ni_3P as shown by the Ni *K*-edge Fourier-transform (FT) spectra in Fig. 3(*c*). These results imply that the as-prepared Ni–P nanoparticles have similar but distorted local atomic structures as compared with the f.c.c.-Ni. It is well known that the position of the *K*-edge is associated with the electron transition from the 1*s* to 3*d* level (Tamaki & Imanaka, 1986; Song *et al.*, 2007) of transition elements. The absorption-edge shift is relevant to the chemical valence of the absorption atom. From Fig. 3(*b*) it can be found that both Ni *K*-edges of the Ni foil and the Ni–P nanoparticles are almost at the same position (E_0 = 8333 eV), but the Ni *K*-edge position of the Ni_3P is slightly higher. This coincidence of the absorption-edge positions between the Ni foil and the Ni–P nanoparticles implies that most of the Ni atoms in the Ni–P nanoparticles

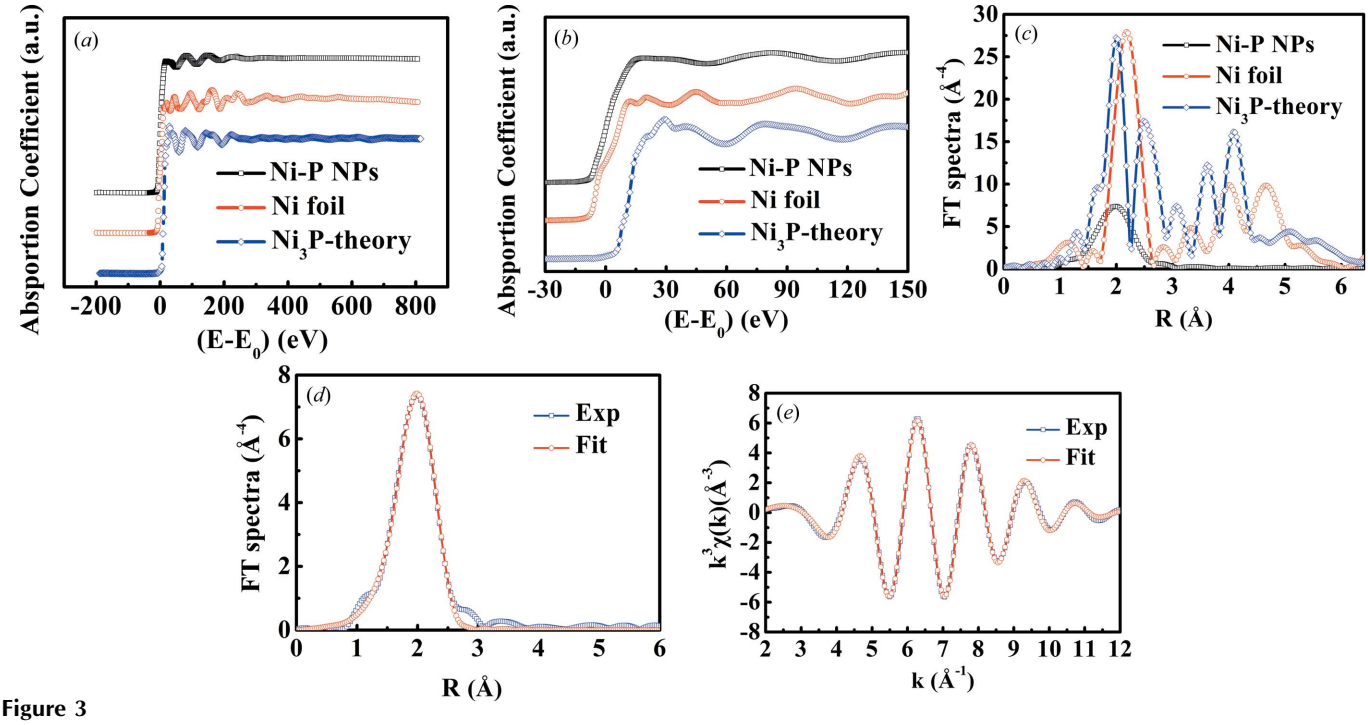

Figure 3
(*a*) Comparison of Ni *K*-edge X-ray absorption spectra collected experimentally from the as-prepared Ni–P nanoparticles (Ni–P NPs) and the Ni foil, as well as the spectrum of Ni_3P calculated theoretically from the crystalline Ni_3P. An enlarged picture near the absorption edge of the three spectra is also displayed (*b*). (*c*) Comparison of Ni *K*-edge Fourier transform spectra corresponding to the three Ni *K*-edge X-ray absorption spectra in (*a*). (*d*) Comparison of Ni *K*-edge Fourier transform spectra between the experimental data and fitting curve with Ni–Ni and Ni–P two sub-shells for the as-prepared Ni–P nanoparticles. (*e*) Comparison of Ni *K*-edge XAFS spectra between the experimental data and fitting curve with Ni–Ni and Ni–P two sub-shells for the as-prepared Ni–P nanoparticles.

have approximately chemical valences of zero. It can also be found that the white-line intensity of the Ni *K*-edge is slightly higher in the Ni–P nanoparticles than in the Ni foil, but slightly lower in the Ni–P nanoparticles than in the crystalline Ni_3P. This phenomenon indicates that there may be more 3*d*-electron state density in the Ni–P nanoparticle than in the Ni foil, but less 3*d*-electron state density in the Ni–P nanoparticle than in the Ni_3P crystal. Perhaps a slight charge transfer occurred between Ni and P atoms of the Ni–P nanoparticles. It was reported that the charge transfer between Ni and P atoms in Ni–P nanoparticles was dependent on the P content (Tamaki & Imanaka, 1986; Fang *et al.*, 1999). When the P content was below 25 at%, the P atom donated electrons to Ni, but the P atom accepted electrons from Ni when the P content was above 25 at%. However, a reverse charge transfer from Ni to P in amorphous Ni–P alloys was also reported (Watanabe *et al.*, 2001). In this study, although the P content in the as-prepared Ni–P nanoparticles is about 21.85 at%, the slight increase of the white line at the Ni *K*-edge XAFS spectrum evidently supports the slight charge transfer from Ni to P atoms. This conclusion is the same as that obtained from the amorphous Ni–P alloys (Anspoks & Kuzmin, 2011). Besides, we also notice that the more complicated oscillation structure in the XAFS spectrum of the pure Ni sample is from the contribution of higher coordination shells; whereas the sinusoidal oscillation profile in the Ni–P nanoparticle XAFS spectrum demonstrates that the higher coordination shells cannot be observed. This is in agreement with the noncrystalline nature of the as-prepared Ni–P nanoparticles as confirmed by the XRD pattern and the TEM image. Such a noncrystalline feature can be clearly observed from the FT spectra of the Ni *K*-edges as shown in Fig. 3(*c*). Different from the pure Ni sample or the crystalline Ni_3P, the higher coordination peaks of the Ni–P nanoparticles have completely disappeared. Compared with bulk Ni foil, an obvious reduction of the magnitude of the coordination peak is observed for the as-prepared Ni–P nanoparticles, which can be attributed to the larger structural disorder and the absence of long-range-ordered structures. Although the smaller particle size can also conduce the magnitude reduction of the FT spectra, a magnitude reduction caused by the nanoscale effects can be excluded since the average size of the as-prepared Ni–P nanoparticles is sufficiently large, over 10 nm (Arčon *et al.*, 2001; Ankudinov *et al.*, 1998). Before a quantitative analysis, the as-prepared Ni–P nanoparticles have been confirmed to have only short-range-ordered structures. Quantitative structural information around the Ni centers can be obtained by fitting the Ni *K*-edge XAFS spectrum. The fitting range in *k*-space is from 2.0 to 12.0 $Å^{-1}$, and the fitting range without phase-shift correction is from 1.0 to 3.0 Å in *R*-space. Figs. 3(*d*) and 3(*e*) show the XAFS fitting curves in *R*-space and in *k*-space, respectively. The reference amplitudes and phase shifts of Ni–Ni and Ni–P atom-pairs were calculated by using the *FEFF* code (Goldman *et al.*, 1988) based on the f.c.c.-structural Ni crystal and the BCT-structural Ni_3P crystal (Watanabe *et al.*, 2001), respectively. During the XAFS fitting process, a

Table 1
Near-neighbor coordination parameters in the noncrystalline Ni–P nanoparticles.

N is the coordination number, *R* is the bond length between the center atom and the backscattering atoms, σ^2 is the Debye–Waller factor, and ΔE is the energy shift of the absorption edge. These parameters are obtained by fitting the Ni *K*-edge and the P *K*-edge XAFS spectra, respectively.

Atom-pair	*N*	*R* (Å)	σ^2 (Å^2) $\times 10^{-3}$	ΔE (eV)
Ni–Ni	9.8 ± 0.4	2.49 ± 0.010	14.4 ± 3.1	−6.2 ± 1.6
Ni–P	2.6 ± 0.3	2.24 ± 0.006	9.25 ± 2.3	−6.1 ± 2.3
P–Ni	8.2 ± 0.5	2.23 ± 0.006	6.85 ± 1.7	6.1 ± 1.2

single Ni–Ni shell was firstly tested, but did not fit the XAFS spectrum well. This is because the Ni–P nanoparticles contain not only the Ni–Ni atom-pairs but also the Ni–P atom-pairs. Therefore, a double-shell fitting of Ni–Ni and Ni–P atom-pairs was used. The fitting curves are also shown in Figs. 3(*d*) and 3(*e*). The fitting parameters are listed in Table 1. On average, each Ni atom in the Ni–P nanoparticles is coordinated by 9.8 Ni atoms and 2.6 P atoms in its nearest neighborhood. The Ni–Ni and Ni–P bond lengths are, respectively, 2.49 Å and 2.24 Å. According to the Ni and P coordination numbers around Ni centers, the P content in the as-prepared Ni–P nanoparticles can be calculated to be about 21 at%, which is very close to the value (21.85 at%) obtained from the ICP-MS analysis. In other words, the Ni–P nanoparticles include 21–22 at% of P and 79–78 at% of Ni.

It is well known that there are 12 Ni near-neighbors coordinated to each Ni center with a Ni–Ni bond length of 2.489 Å in pure f.c.c.-Ni. However, the Ni_3P crystal has three inequivalent sites of Ni. On average, there are three P atoms with an average Ni–P distance of 2.29 Å distributed in the first neighborhood around the Ni center. There are 10.7 Ni atoms with an average Ni–Ni distance of 2.682 Å distributed in the second neighborhood as counting the Ni–Ni atom-pairs within 3 Å. If counting only these Ni–Ni atom-pairs distributed within 2.7 Å, then there are about 6.3 Ni–Ni atom-pairs with an average distance of 2.5845 Å distributed in the second neighborhood around Ni in the Ni_3P crystal. The fitting Ni–Ni distance (2.49 Å) is obviously smaller than these Ni–Ni bond lengths from the second neighborhood of the Ni_3P crystal, but is almost the same as the first-neighbor Ni–Ni bond length (2.489 Å) in the f.c.c.-Ni. Evidently, the coordination environment around the Ni centers in the as-prepared noncrystalline Ni–P nanoparticles is more approaching f.c.c.-Ni. The total coordination numbers of 9.8 Ni–Ni and 2.6 Ni–P are also very close to 12 of f.c.c.-Ni. Therefore, the local atomic structure around Ni in the Ni–P nanoparticles can be attributed to a P-doping f.c.c.-like Ni lattice, and P atoms entered the f.c.c.-lattice by substitution with a doping content of about 21 at%. Moreover, the Ni–P distance (∼2.24 Å) is obviously shorter than the Ni–Ni distance (2.49 Å), which results in a larger mismatch (∼10%) between Ni–Ni and Ni–P bond lengths. Consequently, the Ni–P nanoparticles cannot keep a regular f.c.c. structure. A previous study (Tamaki & Imanaka, 1986) also found that the P-doped f.c.c.-Ni cannot be maintained with good crystallinity when the atomic percentage of P was higher than 14 at%. It is the entrance of smaller P atoms into the f.c.c.-Ni lattice that causes a larger structural distortion and destroys the long-range order of the as-prepared Ni–P nanoparticles.

To obtain the local atomic structure around the P centers, the XAFS spectrum of the P *K*-edge of the as-prepared Ni–P nanoparticles was also collected in fluorescence yield mode. The X-ray absorption spectrum of the P *K*-edge is shown in Fig. 4(*a*). Two main absorption features (A and B) on the P *K*-edge absorption spectrum occurred at 2147.3 and 2153.3 eV as shown in the inset of Fig. 4(*a*), which were assigned to the electronic transitions from P 1*s* to P 3*s* and Ni 4*p* levels, respectively (Watanabe *et al.*, 2001). For comparison, the calculated P *K*-edge absorption spectrum for crystalline Ni_3P is also shown in Fig. 4(*a*). It can be found that both P *K*-edge absorption spectra have quite similar oscillation features except that the experimental spectrum of the as-prepared Ni–P nanoparticles has more disorder and slower oscillation frequency than the calculated spectrum of the crystalline Ni_3P. This similarity between the two spectra implies that the as-prepared Ni–P nanoparticles have quite similar local structure around the P centers as in the crystalline Ni_3P, which supports indirectly the hypothesis that there are some Ni_3P-like ordered structures in the as-prepared Ni–P nanoparticles. It is noticeable that the P *K*-edge XAFS oscillation lasts for at least 400 eV above the absorption edge. The sinusoidal oscillation structure on the P *K*-edge absorption spectrum implies that the distinguishable coordination environments around the P centers are limited to the nearest neighborhood. At the same time, the larger oscillation amplitude indicates that the first near-neighbors around P atoms in the Ni–P nanoparticles are relatively ordered. Indeed, the P *K*-edge XAFS spectrum can be fitted quite well with only one P–Ni shell. The fitting regions are from 2 to 12 Å^{-1} in *k*-space or from 1.4 to 2.6 Å in *R*-space. A single P–P coordination shell or two P–Ni and P–P sub-shells were also, respectively, tested to fit the XAFS spectrum, but the fitting results were not acceptable. This result demonstrates that there is no P–P bonding in the neighborhood of P in the as-prepared Ni–P nanoparticles. A similar conclusion was also reported in a previous study (Tamaki & Imanaka, 1986) for a Ni-rich phosphide. The XAFS fitting curves in *R*-space and *k*-space are, respectively, shown in Figs. 4(*c*) and 4(*d*). The fitting parameters of the P–Ni coordination shell are also listed in Table 1. Within the error bars, the fitting value of the P–Ni (2.231 Å) distance is the same as the fitting value of the Ni–P (2.236 Å) distance although both were independently obtained from the Ni *K*-edge or the P *K*-edge XAFS spectra. This consistency of Ni–P and P–Ni bond lengths convinces us of the reliability of the fitting parameters. The XAFS results demonstrate that there are on average 8.2 Ni atoms surrounding each P center with a P–Ni bond length of 2.23 Å. In crystalline Ni_3P (Watanabe *et al.*, 2001), there are a total of nine Ni near-neighbors surrounding the P center. The nine Ni atoms are distributed with three different P–Ni distances with an average P–Ni bond length of 2.29 Å. The fitting P–Ni distance (2.23 Å) is about 0.06 Å shorter than the average P–Ni bond length (2.29 Å) in

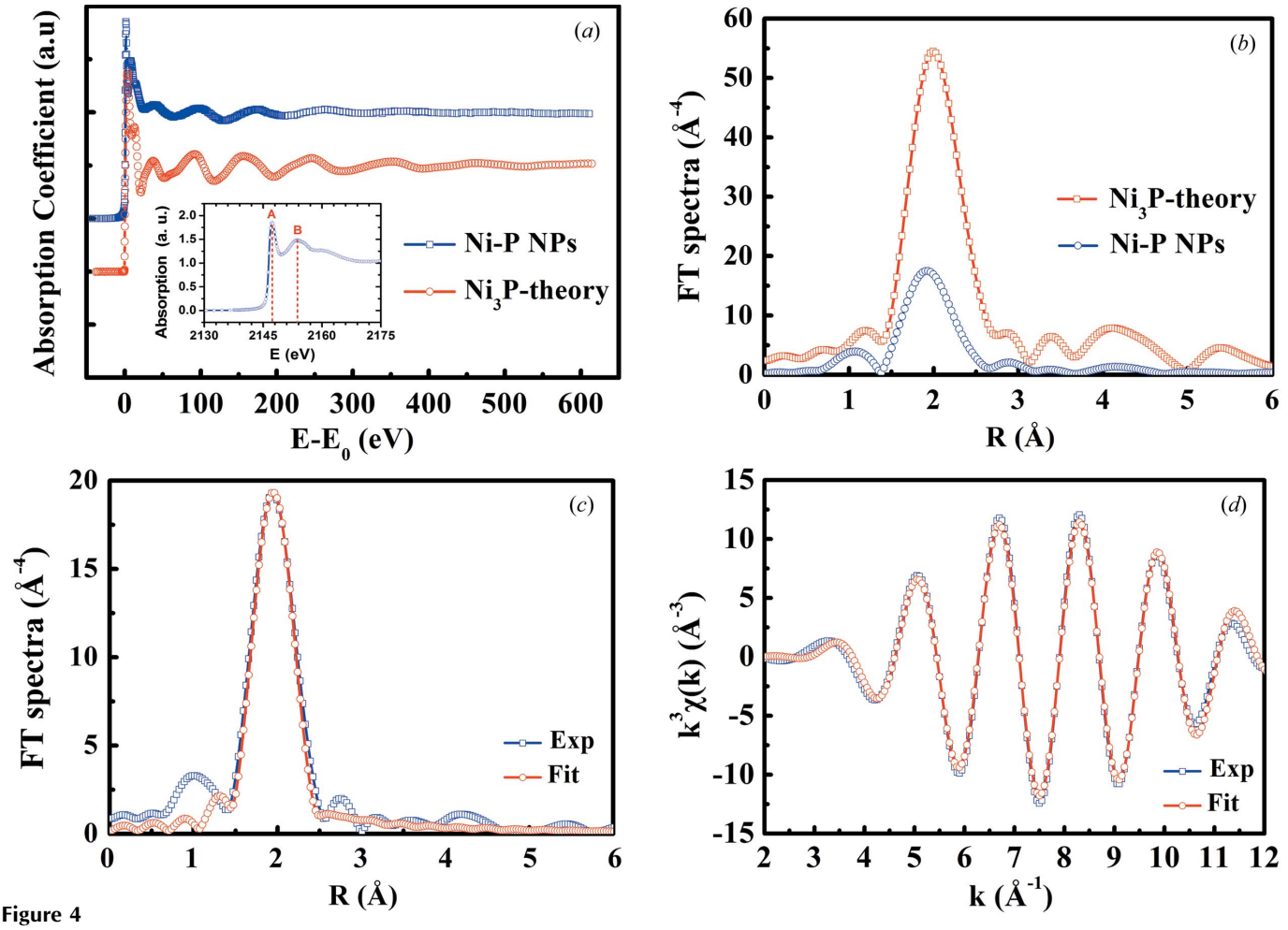

Figure 4
(*a*) Comparison of P *K*-edge X-ray absorption spectra collected experimentally from the as-prepared Ni–P nanoparticles (Ni–P NPs) and calculated theoretically for the crystalline Ni_3P. Two main absorption features occurred at 2147.3 eV (P 1*s* → P 3*p*) and 2153.3 eV (P 1*s* → Ni 4*p*) are shown in the inset. (*b*) Comparison of P *K*-edge Fourier transform spectra corresponding to the two X-ray absorption spectra in (*a*). (*c*) Comparison of P *K*-edge Fourier transform spectra between experimental data and fitting curve with a single P–Ni shell for the as-prepared Ni–P nanoparticles. (*d*) Comparison of P *K*-edge XAFS spectra between the experimental data and fitting curve with a single P–Ni shell for the as-prepared Ni–P nanoparticles.

crystalline Ni_3P. The fitting P–Ni coordination number (8.2) is also slightly smaller than the P–Ni coordination number (9) in crystalline Ni_3P. Evidently, the local coordination environment around the P centers in the as-prepared Ni–P nanoparticles is not completely the same as, but quite similar to, the crystalline Ni_3P.

The above XAFS results confirm again the structural hypothesis about the noncrystalline Ni–P nanoparticles. That is to say, the as-prepared Ni–P nanoparticles can be considered as a 'complex' of P-doped f.c.c.-like Ni centers and Ni_3P-like P centers. We have to emphasize that these Ni centers and P centers are not isolated clusters. A previous study (Goldman *et al.*, 1988) found that two structurally distinct states (Ni_3P and $Ni_{12}P_5$) could exist in two bulk Ni–P glasses, depending on the sample preparation conditions (electrodeposition or pulse electrodeposition). Another study (Lagarde *et al.*, 1983) on amorphous Ni–P alloy demonstrated that the coordination environment around P atoms in the noncrystalline state was very reminiscent of that of the Ni_3P crystalline materials. In this study for the amorphous Ni–P nanoparticles, the coexistence of f.c.c.-like Ni centers and Ni_3P-like P centers explains well the origin of the initial crystal nuclei to form the final crystalline products.

As an additive to the thermal decomposition of AP, the catalytic performance of the as-prepared Ni–P nanoparticles was investigated by DSC measurements. Fig. 5 compares the DSC curves between APs with and without the noncrystalline Ni–P nanoparticles. It can be seen that the DSC curve of pure AP has three obvious features at 245.4, 313.3 and 454.8°C, which are quite similar to previous reports (Vyazovkin & Wight, 1999; Liu *et al.*, 2013). The first feature is an endothermic peak appeared at 245.4°C, which can be attributed to the transformation of AP from the orthorhombic to cubic form. The second feature is an exothermic peak at 313.3°C, which can be attributed to a low-temperature partial decomposition (LTD) of AP. It was reported (Vyazovkin & Wight, 1999) that the LTD of AP stopped as the weight-loss was approximately 30%. The third feature is the high-temperature decomposition (HTD) of AP as observed at 454.8°C. The HTD involves the simultaneous dissociation and sublimation

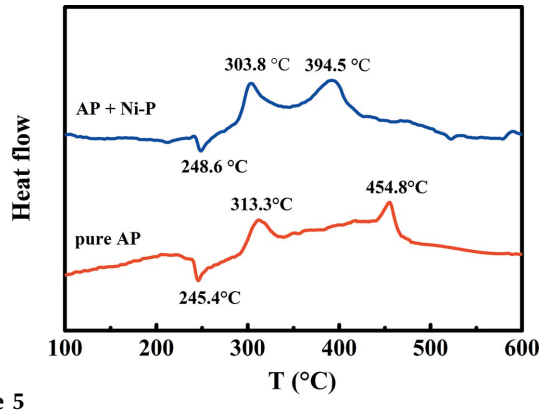

Figure 5
DSC curves of the pure AP and its mixture containing 8.5 wt% of the as-prepared noncrystalline Ni–P nanoparticles.

of AP to $HClO_4$ (g) and NH_4 (g), leading to a complete gasification of AP. Previous research (Lang & Vyazovkin, 2006) observed that the HTD presented also an endothermic peak if the decomposition process took place at ordinary atmosphere under either a flow of inert gas or air, but presented an exothermic peak only when the evolved gases remained in close contact (such as in closed sample pans). This exothermic reaction is due to the oxidation of ammonia by the acid in the gas phase. In our case, the third feature is an exothermic peak because the sample was closed in a pan during the DSC measurements. When 8.5 wt% of the as-prepared noncrystalline Ni–P nanoparticles was added to the sample, the three features still appear on the DSC curve, but showing different trends. The first feature (*i.e.* the endothermic peak at 248.6°C) shows almost no changes in peak position, which indicates that the additive of noncrystalline Ni–P nanoparticles has little effect on the crystallographic transition. The second exothermic feature at 303.8°C has a 9.5°C shift toward lower temperature from 313.3°C, indicating that the addition of noncrystalline Ni–P nanoparticles can decrease the temperature of LTD to a certain degree. An outstanding peak shift took place at the third feature, where the exothermic peak position of the HTD was lowered by 60.3°C from 454.8°C to 394.5°C. These experimental results demonstrate that the as-prepared noncrystalline Ni–P nanoparticles have an obvious catalytic action on the thermal decomposition process of AP, especially on the HTD of AP.

4. Conclusions

The liquid-phase pulse-discharge method has been successfully used to synthesize noncrystalline Ni–P nanoparticles. The local atomic structures and catalytic performance of the as-prepared noncrystalline Ni–P nanoparticles have been studied. The experimental results can be concluded as follows: (i) The as-prepared noncrystalline Ni–P nanoparticles consist of P-doped f.c.c.-like Ni centers and Ni_3P-like P centers. The cross-linkage of these Ni centers and P centers forms a noncrystalline network in the Ni–P nanoparticles. (ii) The locally ordered Ni centers and P centers are the nucleation sites, which can explain well the origin of the initial nuclei to form the final crystalline products after high-temperature annealing. (iii) The as-prepared noncrystalline Ni–P nanoparticles have been validated to have obvious catalytic activity with the decomposition process of APs.

This work was supported by the National Natural Science Foundation of China (Nos. 51374019, U1232203, U1432104, 11405199, 50374010).

References

Ankudinov, A. L., Rehr, J. J. & Conradson, S. D. (1998). *Phys. Rev. B*, **58**, 7565–7576.
Anspoks, A. & Kuzmin, A. (2011). *J. Non-Cryst. Solids*, **357**, 2604–2610.
Arčon, I., Tuel, A., Kodre, A., Martin, G. & Barbier, A. (2001). *J. Synchrotron Rad.* **8**, 575–577.
Boldyrev, V. V. (2006). *Thermochim. Acta*, **443**, 1–36.
Burchardt, T., Hansen, V. & Våland, T. (2001). *Electrochim. Acta*, **46**, 2761–2766.
Chen, Y. Z., She, H. D., Luo, X. H., Yue, G. H. & Peng, D. L. (2009). *J. Cryst. Growth*, **311**, 1229–1233.
Elayaraja, M., Galbokka, H., Layan, S. & Stephanie, L. B. (2011). *ACS Nano*, **5**, 2402–2411.
Fang, Z. G., Shen, B. R., Fan, K. N. & Deng, J. F. (1999). *Acta Chim. Sinica*, **57**, 1246–1251.
Goldman, A. I., Long, G. G., Bennett, L. H., Lashmore, D. S. & Kuriyama, M. (1988). *J. Electrochem. Soc.* **135**, 1919–1921.
Jiang, J. & Kauzlarich, S. M. (2006). *Chem. Mater.* **18**, 435–441.
Kang, X. C., Zhang, J. L., Shang, W., Wu, T., Zhang, P., Han, B., Wu, Z., Mo, G. & Xing, X. (2014). *J. Am. Chem. Soc.* **136**, 3768–3771.
Kawai, T., Bando, K. K., Lee, Y. K., Oyama, S. T., Chun, W. & Asakura, K. (2006). *J. Catal.* **241**, 20–24.
Kawai, T., Sato, S., Chun, W. J., Asakura, K., Bando, K. K., Matsui, T., Yoshimura, Y., Kubota, T., Okamoto, Y., Lee, Y. K. & Oyama, T. S. (2005). *Phys. Scr.* T**115**, 822.
Lagarde, P., Rivory, J. & Vlaic, G. (1983). *J. Non-Cryst. Solids*, **57**, 275–287.
Lang, A. J. & Vyazovkin, S. (2006). *Combust. Flame*, **145**, 779–790.
Li, L., Sun, X., Qiu, X., Xu, J. & Li, G. (2008). *Inorg. Chem.* **47**, 8839–8846.
Liu, L., Li, F., Tan, L., Ming, L. & Yi, Y. (2004). *Propell. Explos. Pyrot.* **29**, 34–38.
Liu, L., Xin, J., Ma, F., Zhi, C. & Li, F. (2013). *Propell. Explos. Pyrot.* **38**, 629–633.
Mandel, K., Dillon, F., Koos, A. A., Aslam, Z., Jurkschat, K., Cullen, F., Crossley, A., Bishop, H., Moh, K., Cavelius, C., Arzt, E. & Grobert, N. (2011). *Chem. Commun.* **47**, 4108–4110.
Maneeprakorn, W., Nguyen, C. Q., Malik, M. A., O'Brien, P. & Raftery, J. (2009). *Dalton Trans.* **58**, 2103–2108.
Mauvernay, B., Doublet, M. L. & Monconduit, L. (2006). *J. Phys. Chem. Solids*, **67**, 1252–1257.
Moreau, L. M., Ha, D. H., Bealing, C. R., Zhang, H., Hennig, R. G. & Robinson, R. D. (2012). *Nano Lett.* **12**, 4530–4539.
Oyama, S. T. (2002). *J. Catal.* **210**, 207–217.
Oyama, S. T., Gott, T., Zhao, H. & Lee, Y.-K. (2009). *Catal. Today*, **143**, 94–107.
Oyama, S. T. & Lee, Y. K. (2008). *J. Catal.* **258**, 393–400.
Shi, G. J. & Shen, J. Y. (2009). *J. Mater. Chem.* **19**, 2295–2297.
Song, J., Wei, Z., Pan, Z., Xie, Z. & Wei, S. (2007). *AIP Conf. Proc.* **882**, 453–456.
Souza, D. C. S., Pralong, V., Jacobson, A. J. & Nazar, L. F. (2002). *Science*, **296**, 2012–2015.
Tamaki, J. & Imanaka, T. (1986). *Chem. Lett.* **15**, 679–682.

Tan, Y. Y., Sun, D. B., Yu, H. Y., Wu, T., Yang, B., Gong, Y., Yan, S., Du, R., Chen, Z., Xing, X., Mo, G., Cai, Q. & Wu, Z. (2014*a*). *J. Alloys Compd.* **605**, 230–236.
Tan, Y. Y., Sun, D. B., Yu, H. Y., Yang, B., Gong, Y., Yan, S., Chen, Z. J., Cai, Q. & Wu, Z. H. (2014*b*). *CrystEngComm*, **16**, 9657–9668.
Tegus, O., Brück, E., Buschow, K. H. J. & de Boer, F. R. (2002). *Nature (London)*, **415**, 150–152.
Tian, N., Zhou, Z. Y., Sun, S. G., Ding, Y. & Wang, Z. L. (2007). *Science*, **316**, 732–735.
Vyazovkin, S. & Wight, C. A. (1999). *Chem. Mater.* **11**, 3386–3393.
Wang, C., Zhang, H., Ye, Y., Shen, R. & Hu, Y. (2013). *Thermochim. Acta*, **568**, 161–164.
Wang, J. W., Johnston-Peck, A. C. & Tracy, J. B. (2009). *Chem. Mater.* **21**, 4462–4467.
Wang, Y., Zhu, J., Yang, X., Lu, L. & Wang, X. (2005). *Thermochim. Acta*, **437**, 106–109.
Watanabe, T., Kato, J., Matsuo, S., Wakita, H. & Umesaki, N. (2001). *X-ray Spectrom.* **30**, 15–20.
Zhao, H. J., Yu, H. Y., Cao, Y. Q. & Sun, D. B. (2010). *J. Univ. Sci. Technol. B*, **32**, 1011.
Zheng, X. F., Yuan, S. L., Tian, Z. M., Yin, S. Y., He, J. H., Liu, K. & Liu, L. (2009*a*). *Chem. Mater.* **21**, 4839–4845.
Zheng, X. F., Yuan, S. L., Tian, Z. M., Yin, S. Y., He, J. H., Liu, K. & Liu, L. (2009*b*). *Mater. Lett.* **63**, 2283–2285.